PCCP

PAPER

View Article Online
View Journal | View Issue

Cite this: *Phys. Chem. Chem. Phys.*, 2017, **19**, 29872

Excited state dynamics for hybridized local and charge transfer state fluorescent emitters with aggregation-induced emission in the solid phase: a QM/MM study†

Jianzhong Fan, Lei Cai, Lili Lin* and Chuan-Kui Wang*

Highly efficient organic light-emitting diodes (OLEDs) based on fluorescent emitters with a hybridized local and charge transfer (HLCT) state have attracted significant attention. Recently, a near-infrared fluorescent compound, 2,3-bis(4′-(diphenylamino)-[1,1′-biphenyl]-4-yl)fumaronitrile (TPATCN), with an HLCT state has been synthetized, and the features of OLEDs based on this compound have been explored. In this study, excited state dynamics of TPATCN in the solid phase has been theoretically studied through a combined quantum mechanics and molecular mechanics (QM/MM) method. By analyzing the changes in geometry, the Huang–Rhys factor, and reorganization energy, non-radiative consumption ways through the torsional motions of diphenylamino and central fumaronitrile in low frequency regions (<200 cm^{-1}) are effectively hindered by the restricted intramolecular rotation (RIR) effect in the solid phase. The fluorescence efficiency of the OLED has been quantitatively calculated. The results show that the fluorescence efficiency is greatly enhanced from 0.16% in the gas phase to 52.1% in the solid phase; this demonstrates the aggregation-induced emission (AIE) mechanism for the OLED. Furthermore, by combining the dynamics of the excited states and the adiabatic energy structures calculated in the solid phase, the so-called hot-exciton process from higher triplet states to a singlet state has been illustrated. Our investigation elucidates the experimental measurement and helps understand the AIE mechanism for HLCT compounds, which is beneficial for developing highly efficient emitters.

Received 25th July 2017,
Accepted 24th October 2017

DOI: 10.1039/c7cp05009g

rsc.li/pccp

1. Introduction

Pure organic thermally activated delayed fluorescent (TADF) materials have attracted significant attention due to their promising application in the construction of highly efficient organic light emitting diodes (OLEDs). OLEDs based on TADF have afforded excellent quantum efficiencies, which are comparable to the results obtained from the best phosphorescent OLEDs.[1–5] Hence, TADF materials have now been regarded as the third-generation emitters for OLEDs after the conventional fluorescent and phosphorescent materials. For designing efficient TADF molecules, one important consideration is that the energy gap between the first singlet excited state (S_1) and the first triplet excited state (T_1) should be small enough for reverse conversion from T_1 to S_1; thus, the electro-generated singlet and triplet excitons can be fully used. Ideally, the maximum internal quantum efficiency (IQE) of TADF-OLEDs can approach 100%.[6,7] An effective way to decrease the S_1–T_1 energy gap is connecting suitable donor (D) and acceptor (A) groups by a sterically hindered, such as a bulky, twisted, or U-shaped, structure because this can effectively prevent the spatial overlapping between the highest occupied molecular orbital (HOMO) and lowest unoccupied molecular orbital (LUMO).[8–11] However, one negative effect is inevitably generated: small orbital overlap for S_1 with a charge transfer (CT) feature causes a slow radiative rate and low luminescence efficiency. Thus, first, how to balance the relationship between the small S_1–T_1 gap for realizing efficient reverse intersystem crossing (RISC) and fast radiative rate for achieving high luminescence efficiency should be considered. In this regard, a number of valid ways have been proposed. Adachi's group has found that the fluorescence rate can be enhanced by inserting a π unit between D and A units.[12] Ma's group has put forward the hybridized local and charge transfer (HLCT) excited state. The HLCT state is a new special category in the excited state, which combines both local excited (LE) and charge transfer (CT) characters into a new species.[13–15] Thus, two compatible characteristics, high-efficiency fluorescence radiation from the LE

Shandong Province Key Laboratory of Medical Physics and Image Processing Technology, Institute of Materials and Clean Energy, School of Physics and Electronics, Shandong Normal University, 250014 Jinan, China.
E-mail: ckwang@sdnu.edu.cn, linll@sdnu.edu.cn

† Electronic supplementary information (ESI) available. See DOI: 10.1039/c7cp05009g

state and a weakly bound exciton, which is responsible for the full exciton utilization from the CT state, are combined. Therefore, the HLCT state provides a novel approach for the design of highly efficient D–A type compounds. Second, TADF materials are usually doped into appropriate host matrices to mitigate the concentration quenching and exciton annihilation processes, which bring serious efficiency roll-off at a high luminance and impede the efficiency enhancement of OLEDs. Aggregation-induced emission (AIE) is regarded as a promising strategy to solve the quenching and annihilation problems.[16–18] Usually, AIEgens are weak emitters in dilute solutions, but become highly efficient emitters in rigid environments, such as water or solid film. To date, many AIE materials have been extensively studied and employed to fabricate efficient, stable, and simplified non-doped fluorescent OLEDs.[19–22] Third, another significant negative factor is that red and near-infrared (NIR) TADF emitters typically show relatively low luminescence efficiency due to their large non-radiative decay rates that increase exponentially with an increase in the emission wavelength, as governed by the energy gap law.[23,24] Recently, a D–A type NIR fluorescent compound, 2,3-bis(4′-(diphenylamino)-[1,1′-biphenyl]-4-yl) fumaronitrile (TPATCN), has been synthesized and fully characterized by Lu *et al.*[25] TPATCN exhibits strong NIR fluorescence, and the external quantum efficiency of non-doped NIR OLED reaches 2.58%, which is among the highest values reported of NIR OLEDs. Thus, theoretical investigations to reveal the inner AIE and HLCT mechanisms for red or NIR emitters in the solid phase are necessary to develop highly efficient non-doped OLEDs.

Herein, we performed a detailed study on the photoelectric properties of the TPATCN molecule to investigate the AIE and HLCT mechanisms (shown in Fig. 1a) based on the first-principles calculations. The environmental effect of the molecule in film is focused using the combined quantum mechanics and molecular mechanics (QM/MM) method. Based on the thermal vibration correlation function (TVCF), the non-radiative rate as well as the intersystem crossing (ISC) and reverse intersystem crossing (RISC) rates have been calculated. Further, the excited state dynamics for TPATCN with HLCT and AIE mechanisms in the solid phase has been illustrated, and experimental measurements have been reasonably elucidated.

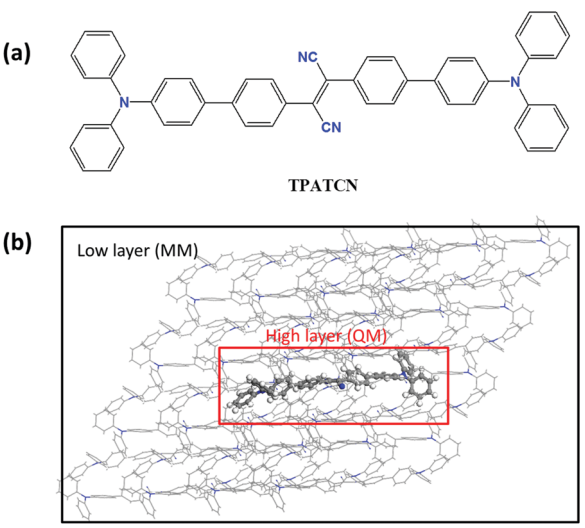

Fig. 1 (a) Chemical structure of TPATCN. (b) ONIOM model: surrounding molecules are regarded as the low layer and the centered TPATCN is treated as the high layer.

2. Computational details

The prompt fluorescence efficiency Φ_{PF} is determined by the competition between the radiative decay rate (k_r) and the non-radiative decay rate (k_{nr}) from S_1 to S_0 as well as the ISC (k_{ISC}) rate between the singlet and triplet excited states according to the equation $\Phi_{PF} = \frac{k_r}{k_r + k_{nr} + k_{ISC}}$. Thus, by either increasing the radiative rate or suppressing the non-radiative rate, high fluorescence efficiency can be achieved. Therefore, theoretical calculations of radiative and non-radiative rates play an important role in predicting luminous efficiencies.

As is known, the excited state properties of D–A type molecules are functional dependent; thus, an appropriate functional should be selected first. Recently, some ingenious approaches such as the LC-wPBE and LC-BLYP method, NTO method, and optimal Hartree–Fock (OHF) method have been proposed and applied.[26–30] In our study, the emission wavelengths of the TPATCN molecule in gas and solid phases have been calculated using functionals with different percentages of HF exchange (HF%) component. Herein, the emission wavelengths calculated using the functionals with different HF% are shown in Table 1. The emission wavelengths calculated with the LC-wPBE (ω = 0.176833) and LC-BLYP (ω = 0.179843) functionals in both gas and solid phases are much smaller than the experimental values. Moreover, the emission wavelength of the molecule in the solid state calculated with the PBE0 functional is 661 nm, which is in better agreement with the experimental values (670 nm in film and 622 nm in powder and crystal). Consequently, the PBE0 functional with the 6-31G(d) basis set is adopted in our latter calculations.

To simulate the properties of a molecule in the solid state, a combination of quantum mechanics and molecular mechanics (QM/MM) method with a two-layer ONIOM approach is used.[31,32] Based on the X-ray structure, a computation model has been

Table 1 Emission wavelength calculated by adopting different functionals for studied molecule in the gas and solid phase is listed

	HF%	Gas (nm)	Solid (nm)
O3LYP	11.61	1027	1077
B3LYP	20	773	774
PBE0	25	662	**661**
BMK	42	552	542
M062X	54	523	506
wB97XD		540	490
LC-wPBE		555	526
LC-BLYP		547	535
Film[a]		—	**670**
Powder[a]		—	**622**
Crystal[a]		—	**622**

[a] Experimental data.

constructed, as shown in Fig. 1b. The central TPATCN is regarded as a high layer and calculated by the QM method. The surrounding molecules are treated as the MM section and are defined as the low layer. Universal force field (UFF) is used for the MM part, and the electronic embedding is adopted in the QM/MM calculation. Moreover, the molecules of the MM part are frozen, and only the QM section is free during the QM/MM geometry optimizations for the S_0, S_1, T_1, and T_2 states. All these calculations are carried out using the Gaussian 09 package.[33] Further, the normal mode analyses have been performed by the DUSHIN program.[34] Based on the electronic properties, the radiative and non-radiative decay rates as well as the ISC and RISC rates in the gas and solid phase have been calculated using MOMAP (Molecular Materials Property Prediction Package), which shows superiority in describing and predicting optical properties of polyatomic molecules.[35–39] The methodology details are provided in the ESI.†

3. Results and discussions

3.1 Geometry and photophysical properties

As is known, the molecular geometry of a state determines both its electronic structure and photophysical properties. Thus, the geometry of the S_0 state has been optimized by the DFT method at the PBE0/6-31G(d) level, and the photophysical properties of the excited states (S_1, T_1, and T_2) have been determined by the TD-DFT method. The atomic labels, interesting dihedral angles, and the index of the phenyl ring are shown in Fig. S1 (ESI†), and the corresponding data are presented in Table 2. In the gas phase, the geometry differences between S_0 and S_1 are mainly caused by changes in $\theta7$, $\theta8$, and $\theta9$. Moreover, the variations in $\theta7$, $\theta8$, and $\theta9$ account for the main part when a molecule transfers between S_1 and T_1. $\theta8$ changes by about 65.6°; this indicates a large geometry difference. Small geometry changes are found between S_1 and T_2; this means S_1 and T_2 have a similar configuration. On the other hand, for a molecule in the solid phase, restricted geometry changes can be found, especially for dihedral angles of $\theta7$, $\theta8$, and $\theta9$. Since the geometry differences between S_0 and S_1 as well as between S_1 and T_1 (T_2) have a close relationship with the excited state dynamics such as the non-radiative decay and ISC (RISC) processes, intuitive comparisons of the geometries were made, as shown in Fig. S2 (ESI†). The root of the mean of squared displacement (RMSD) with the expression $\mathrm{RMSD} = \sqrt{\frac{1}{N}\sum_{i}^{n\mathrm{atom}}\left[(x_i - x_i')^2 + (y_i - y_i')^2 + (z_i - z_i')^2\right]}$ is an effective tool to quantitatively characterize the geometric changes, and the value of RMSD between two states is calculated using Multiwfn.[40] It has been found that the geometric changes between S_0 and S_1 in the gas phase are more significant than those in the solid phase, and the RMSD is 0.624 Å and 0.143 Å, respectively. Thus, the non-radiative energy consumption path is hindered, and enhanced fluorescence efficiency can be expected in the solid phase. Moreover, a large RMSD value of 2.618 Å between S_1 and T_1 in the gas phase is found, which means a large geometry change between two states. However, a decreased RMSD value (0.193 Å) between S_1 and T_1 is found in the solid phase due to intermolecular interaction in rigid environments. Moreover, S_1 and T_2 maintain a similar configuration whether in the gas (RMSD = 0.042 Å) or in solid phase (RMSD = 0.064 Å), and this indicates a small variation in reorganization energy for the ISC and RSIC processes.

To gain deep insights into the photophysical properties in the gas and solid phases, the frontier molecular orbitals have been examined and are plotted in Fig. 2. In the gas phase, it can be easily seen that the HOMO is distributed on the whole molecule with sizeable distribution on two diphenylamino units, and the LUMO is mainly localized in the central fumaronitrile core and two central connected phenyl rings. In the solid phase, the distribution of HOMO is mainly in the right section of the molecule, and the distribution of LUMO remains almost unchanged, with both increased orbital energy of HOMO and LUMO as compared to that in the gas phase. To characterize the nature of T_1 and T_2, natural transition orbital (NTO) analysis has been performed. The highest occupied NTO (HONTO) and lowest unoccupied NTO (LUNTO) with transition ratios are shown in Fig. S3 (ESI†). Thus, the transition nature of S_1, T_1, and T_2 is HLCT, LE, and HLCT states, respectively, in the gas phase, whereas it changes to CT, LE, and HLCT states in the solid phase. The change in the transition nature for S_1 from the gas (HLCT) to solid phase (CT) is caused by the unbalanced intermolecular interaction between the two terminal diphenylamino units. To visualize the interactions between the QM and MM molecules, a reduced density gradient (RDG) function has been applied.[41,42] As shown in Fig. S4 (ESI†), more obvious intermolecular interactions can be found in closely packed units. Thus, unbalanced intermolecular interactions between

Table 2 Geometry parameters of S_0, S_1, T_1, and T_2 states for TPATCN in the gas and solid phase. θ (marked in Fig. S1, ESI) is the dihedral angle. Δ represents the variation between two states

	Gas							Solid						
Geometry	S_0	S_1	T_1	T_2	$\lvert\Delta_{S_0-S_1}\rvert$	$\lvert\Delta_{S_1-T_1}\rvert$	$\lvert\Delta_{S_1-T_2}\rvert$	S_0	S_1	T_1	T_2	$\lvert\Delta_{S_0-S_1}\rvert$	$\lvert\Delta_{S_1-T_1}\rvert$	$\lvert\Delta_{S_1-T_2}\rvert$
$\theta1$	66.7	69.7	65.7	69.4	3.0	4.0	0.3	60.6	65.7	58.2	62.3	5.1	7.5	3.4
$\theta2$	112.8	110.4	113.0	110.5	2.4	2.6	0.1	108.5	105.1	108.7	107.4	3.4	3.6	2.3
$\theta3$	146.0	147.3	149.0	148.0	1.3	1.7	0.7	156.8	146.3	155.7	151.3	10.5	9.4	5.0
$\theta4$	−145.4	−143.8	−149.7	−146.2	1.6	5.9	2.4	−150.2	−151.9	−157.1	−154.1	1.7	5.2	2.2
$\theta5$	66.5	68.9	65.9	67.9	2.4	3.0	1.0	70.8	71.5	71.1	70.0	0.7	0.4	1.5
$\theta6$	67.1	68.9	67.2	68.4	1.8	1.7	0.5	58.9	59.4	58.7	58.8	0.5	0.7	0.6
$\theta7$	147.4	162.0	179.4	161.4	14.6	17.4	0.6	160.3	164.6	174.5	165.4	4.3	9.9	0.8
$\theta8$	169.0	156.7	91.1	156.1	12.3	65.6	0.6	164.5	157.6	140.6	157.1	6.9	17.0	0.5
$\theta9$	147.9	159.4	179.4	160.3	11.5	20.0	0.9	157.7	160.5	172.1	161.0	2.8	11.6	0.5

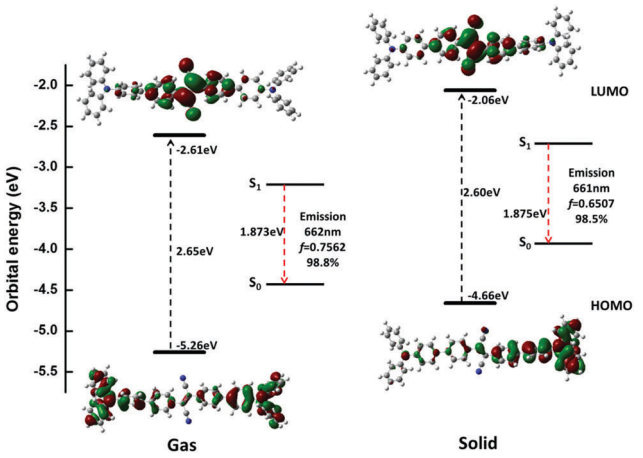

Fig. 2 Spatial distributions of HOMO and LUMO as well as their orbital energies for TPATCN in the gas (left) and solid phase (right). Emission wavelength and oscillator strength are shown in the insets.

the two terminal diphenylamino units are generated. Moreover, T_1 is an LE state, and it can provide stable energy. On the other hand, T_2 is an HLCT state whether in the gas or solid phase, and it can provide a hot exciton channel with excitons transferring from T_2 to S_1. More evidence is shown in Fig. 3, and the adiabatic excitation energies for S_1, S_2, T_1, T_2, and T_3 have been calculated in both the gas and solid phase by optimizing their geometry structures. In the gas phase, the S_1–T_1 energy gap is 0.87 eV, and the S_1–T_2 energy gap is 0.04 eV. In the solid phase, the S_1–T_1 energy gap is 0.58 eV, and the S_1–T_2 energy gap is 0.003 eV. Thus, a large S_1–T_1 energy gap (ΔE_{st}) indicates that TADF cannot be observed due to the blocked RISC process from T_1 to S_1 according to the equation $k_{RISC} \propto \exp\left(\frac{-E_{st}}{K_B T}\right)$. Moreover, this small S_1–T_2 energy gap can efficiently promote the RISC process from T_2 to S_1, and a hot exciton process is generated. This process for OLEDs shows advantages over the cold exciton process, which suffers from the problems of triplet–triplet annihilation (TTA) and singlet–triplet quenching due to the accumulated T_1 excitons. In the hot exciton process, high level triplet excitons can quickly be transferred to singlet states, and the accumulation of triplet excitons in the T_1 state can be avoided. Thus, we know that intermolecular interaction can affect the geometry structures and further generate different photophysical properties. Furthermore, we believe that the easily available modification of the central fumaronitrile core can provide a new and promising opportunity for the design and construction of HLCT materials towards highly efficient OLEDs.

3.2 The Huang–Rhys factor and reorganization energy

To figure out the structure–property relationship during the energy conversion processes $S_1 \rightarrow S_0$, the Huang–Rhys (HR) factor, which can characterize the modification of vibrational quanta while going from one electronic state to another, has been calculated by the equation $HR_k = \frac{w_k D_k^2}{2}$, where ω_k is the vibration frequency and D_k is the normal coordinate displacement of mode k. We analyzed the HR factors as well as the displacement vectors of the vibration modes with the largest HR factors in the gas and solid phase. The corresponding data are shown in Fig. 4a and b. For the decay process in the gas phase, the large HR factors 10.1 (5.70 cm^{-1}), 11.2 (8.38 cm^{-1}), and 3.1 (43.69 cm^{-1}) correspond to the torsional motions (shown as insets) of diphenylamino and central fumaronitrile in low frequency regions (<200 cm^{-1}). The HR factors in the solid phase are decreased with the large factors being 0.73 (32.85 cm^{-1}) and 0.59 (66.01 cm^{-1}). The calculation results indicate that the rotational motions in low frequency regions (<200 cm^{-1}), especially for the central fumaronitrile moiety, are hindered in the solid phase due to intermolecular interaction. Thus, the non-radiative energy consumption way through rotation is suppressed by the restricted intramolecular rotation (RIR) effect, and enhanced fluorescent efficiency can be expected in the solid phase. In addition, the reorganization

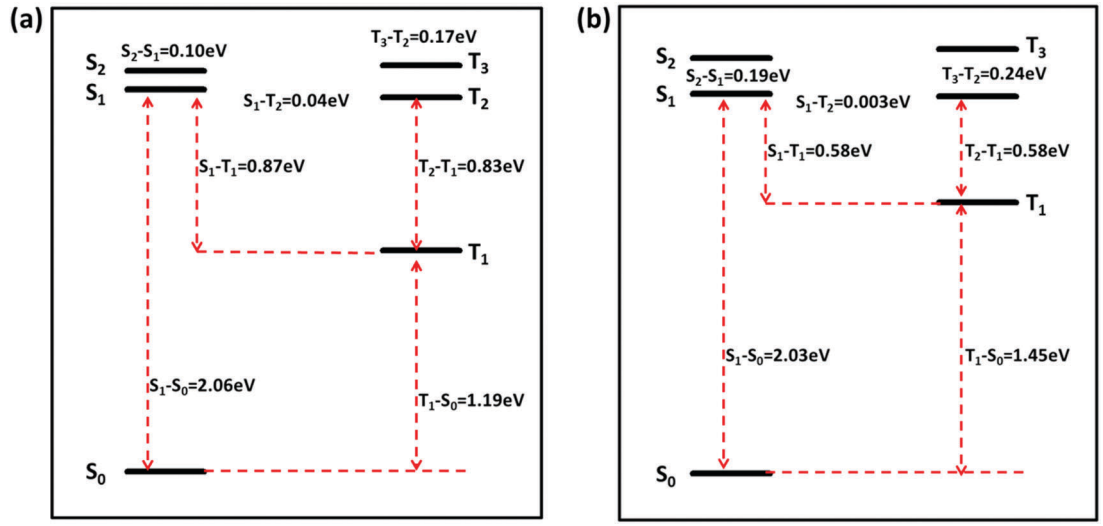

Fig. 3 Adiabatic excitation energies for TPATCN in the gas (a) and solid phase (b).

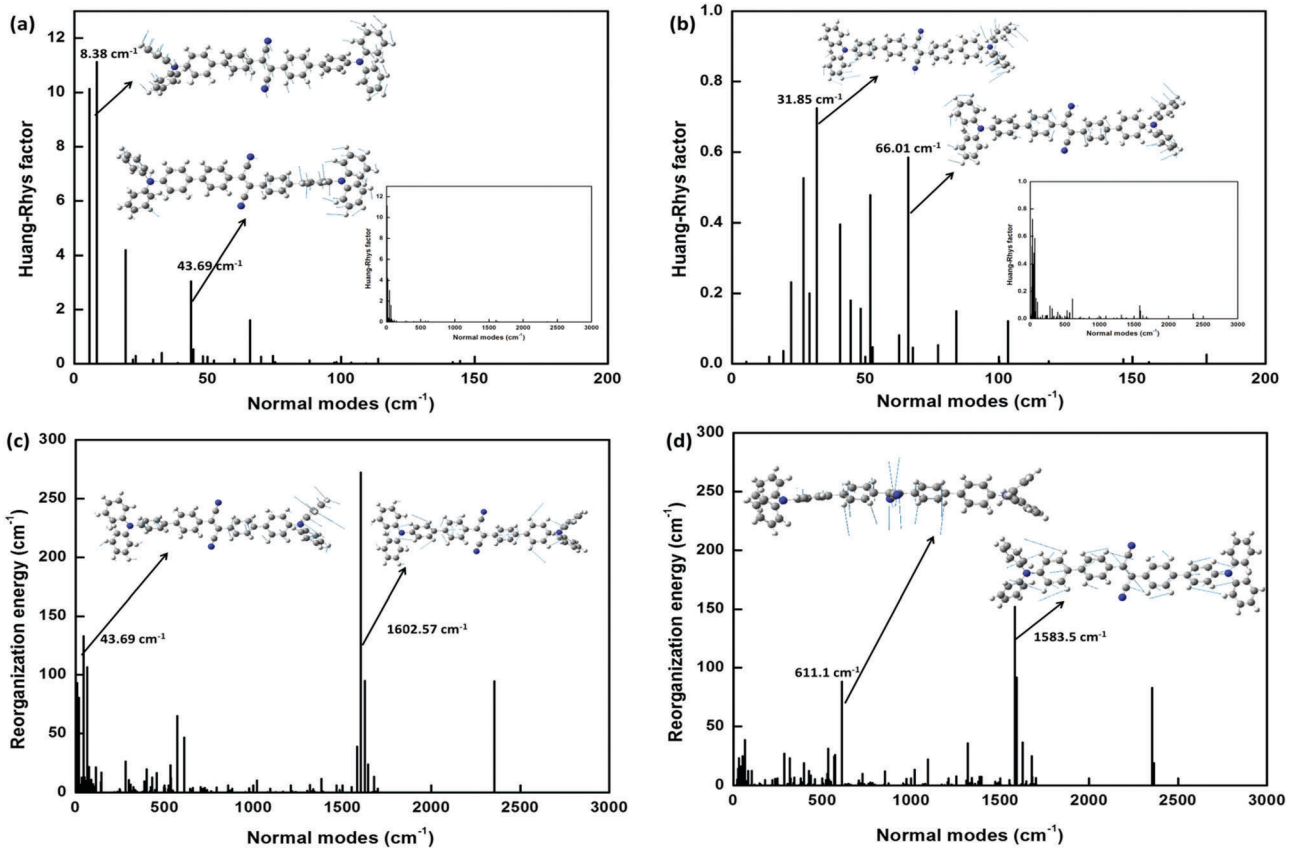

Fig. 4 Calculated HR factors *versus* the normal mode frequencies in the gas (a) and solid phase (b) as well as the reorganization energies *versus* the normal mode frequencies in the gas (c) and solid phase (d). Representative vibration modes are shown in the insets.

energies $(=\sum_k w_k \mathrm{HR}_k)$ *versus* the normal mode frequencies in the gas and solid phase are shown in Fig. 4(c) and (d), respectively. In low frequency regions, the reorganization energies are decreased and show a trend similar to that of HR factors. Moreover, the C=C stretching vibration in high frequency regions is restricted, with the reorganization energy being 33.7 meV (1602.57 cm^{-1}) in the gas phase and 18.9 meV (1583.50 cm^{-1}) in the solid phase. For better understanding the relationship between photophysical properties and molecular structures, we projected the reorganization energies onto the internal coordinate of the molecule. Contributions from bond lengths, bond angles, and dihedral angles are demonstrated in Fig. 5, and the corresponding data are presented in Table 3. In the gas phase, reorganization energy is mainly contributed by the dihedral angle, and its value is 100.7 meV (48.9%). On the other hand, for the molecule in the solid phase, the contribution from bond length (87.2 meV) forms the main part (56.9%). Thus, the decrease in the reorganization energy from the gas to solid phase mainly originates from the decrement contributed by the dihedral angle (56.4 meV) that is associated with the torsional motion of central fumaronitrile and diphenylamino in low frequency regions.

Therefore, a detailed analysis for the variation in HR and reorganization energy when the molecule transfers from the gas to solid phase reveals that the non-radiative consumption ways through the torsional motions of diphenylamino and

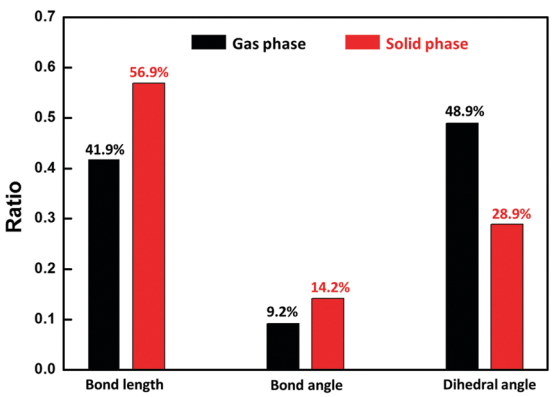

Fig. 5 Contribution to the reorganization energy from bond length, bond angle, and dihedral angle in the gas (black) and solid phase (red).

Table 3 Reorganization energies (meV) from bond length, bond angle, and dihedral angle in the gas and solid phase are listed. $\Delta_{\mathrm{Gas-Solid}}$ represents the energy difference between the gas and solid phase

	Gas	Solid	$\Delta_{\mathrm{Gas-Solid}}$
Bond length	86.2	87.2	−1.0
Bond angle	19.0	21.8	−2.8
Dihedral angle	100.7	44.3	56.4
Total	205.9	153.3	52.6

central fumaronitrile in low frequency regions are effectively hindered by the RIR effect caused by intermolecular interaction in the solid phase. Thus, the aggregation-induced emission (AIE) mechanism is revealed for TPATCN. Actually, there is not the only RIR mechanism for the AIE feature. Recently, Blancafort and Liu *et al.* introduced a restricted access to a conical intersection (RACI) model to explain the AIE mechanism, and this needed high-level *ab initio* quantum-chemical calculations.[43–46] Moreover, non-adiabatic dynamics simulation to investigate the non-radiative decay processes for AIE molecules is applied.[47] The effect of the abovementioned mechanisms on the non-radiative decay process is more complicated when they are tangled together. In our studies, the luminescence quantum yield in the solid phase (52.1%) is much larger than that in the gas phase (0.16%). Although both values are overestimated because the possibly more efficient non-adiabatic transition *via* this intermediate has not been considered, a very large difference between these two luminescence quantum yields is expected. Thus, the AIE mechanism is demonstrated.

3.3 Excited state dynamics in the solid phase

To study the excited state dynamics, adiabatic excitation energies and spin–orbit coupling (SOC) effect should be considered. Based on the first-principles calculations, the SOC constants (with the unit of cm^{-1}) between S_1 and two lowest triplet excited states (T_1 and T_2) both in the gas and solid phase are calculated using the Dalton2013 package.[48] The corresponding data are listed in Table 4. In the gas phase, it can be found that the SOC constants (0.17 cm^{-1} and 0.05 cm^{-1}) for the ISC process based on the S_1 structure are smaller than those based on T_1 (2.55 cm^{-1}) and T_2 (0.06 cm^{-1}) for the RISC process. On the other hand, for the molecule in the solid phase, the SOC values are weakly changed. Based on the methodology illustrated in the ESI,† the radiative (K_r) and non-radiative (K_{nr}) rates from S_1 to S_0, the ISC (K_{ISC}) and RISC (K_{RISC}) rates between singlet and triplet excited states, the internal conversion rate (K_{IC}) from T_2 to T_1, and the phosphorescence rate (K_P) and the non-radiative rate from T_1 to S_0 in both the gas and solid phases are calculated to elaborate the excited state dynamics. Further, the prompt fluorescence and ISC efficiencies are obtained. The corresponding data are listed in Table 5. It can be seen that the radiative decay rate K_r is smaller in the solid phase (9.94×10^7 S^{-1}) than that in the gas phase (1.15×10^8 S^{-1}) due to the decreased oscillator strength caused by the localized HOMO in the solid phase. The non-radiative decay rate K_{nr} from S_1 to S_0 is 7.02×10^{10} S^{-1} in the gas phase, which is two orders of magnitude larger than K_r (1.15×10^8 S^{-1}).

Table 4 Calculated spin orbit coupling constants (in cm^{-1}) between selected singlet and triplet excited states for TPATCN in the gas and solid phase based on the optimized S_1, T_1, and T_2 structures

	Gas		Solid	
Geometry	$\langle S_1\|Hso\|T_1\rangle$	$\langle S_1\|Hso\|T_2\rangle$	$\langle S_1\|Hso\|T_1\rangle$	$\langle S_1\|Hso\|T_2\rangle$
S_1	0.17	0.05	0.16	0.06
T_1	2.55	—	0.14	—
T_2	—	0.06	—	0.07

Table 5 Calculated radiative and nonradiative rates from S_1 (T_1) to S_0 as well as the ISC and RISC rates between singlet and triplet excited states, and the calculated prompt fluorescence efficiency (Φ_{PF}), ISC efficiency (Φ_{ISC}) are listed. Corresponding experimental results are also presented with the superscript 'exp'

	Gas	Solid
$K_r(S_1 \rightarrow S_0)$	1.15×10^8	9.93×10^7
$K_{nr}(S_1 \rightarrow S_0)$	7.02×10^{10}	8.40×10^7
$K_{ISC}(S_1 \rightarrow T_1)$	1.47×10^6	3.96×10^6
$K_{ISC}(S_1 \rightarrow T_2)$	8.60×10^5	3.61×10^6
$K_{RISC}(T_1 \rightarrow S_1)$	4.22×10^{-1}	1.75×10^{-4}
$K_{RISC}(T_2 \rightarrow S_1)$	5.00×10^4	2.81×10^5
$K_{IC}(T_2 \rightarrow T_1)$	6.92×10^7	7.22×10^{12}
$K_p(T_1 \rightarrow S_0)$	5.71×10^2	1.08×10^{-3}
$K_{nr}(T_1 \rightarrow S_0)$	2.29×10^7	4.03×10^5
Φ_{PF}	0.16%	52.1%
Φ_{ISC}	0.003%	4.0%
Φ_{PF}^{exp}	----	72%

Thus, weak emission can be found for the isolated molecule. For the molecule in the solid phase, the value of K_{nr} is 8.40×10^7 S^{-1} and becomes comparable to the radiative decay rate (9.94×10^7 S^{-1}). Consequently, efficient emission can be expected. The log K_{nr} (ΔE) parabola is shown in Fig. S5 (ESI†); no vibrational feature is found in the gas and solid phase; this indicates the accuracy of the calculated K_{nr}. As a result, the significant decrease in the non-radiative rate in the solid phase is caused by the enhanced intermolecular interactions.

Through the adiabatic energy landscape (Fig. 3), we know that the ISC and RISC processes mainly occur between S_1 and T_1 as well as T_2. Thus, both the ISC and RISC rates between S_1 and T_1 (T_2) are calculated. It is found that the ISC from S_1 to T_1 or from S_1 to T_2 in the solid phase is slightly increased as compared to that in the gas phase. This is due to the decreased S_1–T_1 and S_1–T_2 energy gaps as well as the comparable SOC constants (0.17 and 0.05 in the solid phase and 0.16 and 0.06 in the gas phase). The RISC process mainly occurs from T_2 to S_1, and the transition from T_1 to S_1 can be neglected because of the large S_1–T_1 energy gap although considerable SOC is found between them. Thus, the hot exciton process is generated. Further, the internal conversion rate (K_{IC}) from T_2 to T_1 and the radiative (K_P) as well as the non-radiative decay rates from T_1 to S_0 are calculated. Due to the decreased T_2–T_1 gap and the increased T_1–S_0 gap, the $K_{IC}(T_2$–$T_1)$ in the solid phase (7.22×10^{12} S^{-1}) is five orders of magnitude larger than that in the gas phase (6.92×10^7 S^{-1}), and $K_{nr}(T_1$–$S_0)$ in the solid phase (4.03×10^5 S^{-1}) becomes two orders of magnitude smaller than that in the gas phase (2.29×10^7 S^{-1}). Moreover, for the TPATCN molecule with red fluorescence emission, the reported exciton utilization is 39%.[25] The energy gap between T_2 and T_1 is calculated to be 0.58 eV, which is quite different from that for their other reported HLCT molecules.[49] This results in a larger internal conversion (IC) rate from T_2 to T_1. As a result, the exciton utilization is smaller than 100%. Thus, for this kind of HLCT molecule, another mechanism for exciton utilization originates from triplet–triplet annihilation (TTA) that enhances the red fluorescence emission.

Moreover, to determine how conversion occurs between S_1 and T_2, we first analyzed the energy landscape (shown in Fig. 3).

It shows that no additional triplet level is found between S_1 and T_2. Thus, the conversion pathway through intermediate states is excluded. Furthermore, as the torsion of the unhindered C=C double bond (the central bond of the fumaronitrile moiety) is easily caused by photo-excitation in gas and solution, the potential energy surfaces (PESs) of S_1 and T_2 along the dihedral angle ($\theta 8$ in Fig. S1, ESI†) of the central fumaronitrile unit are calculated. As shown in Fig. S6 (ESI†), the crossing points between two PESs occur at about $\theta 8 = 11^\circ$ and 24°. Both the S_1 and T_2 states need large energies to reach the first crossing point. Therefore, conversion pathway through the crossing point is difficult to occur. Since the calculated energy gap between S_1 and T_2 is very small, the direct ISC between S_1 and T_2 has been estimated in this study.

Based on the abovementioned results, the prompt fluorescent efficiency (Φ_{PF}) in the solid phase is 52.1%, which is consistent with the experimental value (72%). Moreover, Φ_{PF} is 0.16% for the isolated molecule; this elaborates the AIE mechanism. In addition, the calculated ISC efficiency Φ_{ISC} is 4.0% in the solid phase. Theoretical results based on the first-principles calculations in the solid state show good agreement with the experimental results; this confirms the HLCT and AIE mechanisms of the TPATCN molecule.

4. Conclusion

In this study, we have theoretically investigated the excited state dynamics of the near-infrared HCLT compound TPATCN in the solid phase using the QM/MM method. According to the results of the comparison of the molecular geometries of S_0 and S_1 states, geometrical changes in the solid phase are restricted due to the enhanced intermolecular interaction. The small S_1–T_2 gap (0.003 eV) in the solid phase can efficiently promote the RISC process from T_2 to S_1. By analyzing the HR factors and reorganization energies, the non-radiative consumption ways *via* the torsional motions of diphenylamino and central fumaronitrile in low frequency regions (<200 cm^{-1}) are effectively hindered by the restricted intramolecular rotation effect in the solid phase. The aggregation-induced emission mechanism is revealed for the TPATCN compound, and the fluorescence efficiency is enhanced from 0.16% in the gas phase to 52.1% in the solid phase. Furthermore, the suggested hot-exciton process of the HLCT emitters in OLEDs is illustrated by combining the dynamics of the excited states and the adiabatic energy structures calculated in the solid state. Our investigation can help understand the HLCT and AIE mechanisms of the TPATCN emitter and design more efficient OLEDs.

Conflicts of interest

There are no conflicts of interest to declare.

Acknowledgements

This work was supported by the National Natural Science Foundation of China (Grant No. 11374195 and 21403133). The authors acknowledge the support provided by the Taishan Scholar Project of Shandong Province and the Scientific Research Foundation of the Shandong Normal University. The authors express thanks to the support provided by the Promotive Research Fund for Excellent Young and Middle-aged Scientists of Shandong Province (Grant No. BS2014CL001) and the General Financial Grant from the China Postdoctoral Science Foundation (Grant No. 2014M560571). Many thanks to Professor Yi Luo, Professor Zhigang Shuai and Qian Peng for their helpful suggestions in our calculation. Thanks to Professor Yingli Niu for his great help with the usage of MOMAP.

References

1 H. Uoyama, K. Goushi, K. Shizu, H. Nomura and C. Adachi, *Nature*, 2012, **492**, 234.
2 Q. Zhang, J. Li, K. Shizu, S. Huang, S. Hirata, H. Miyazaki and C. Adachi, *J. Am. Chem. Soc.*, 2012, **134**, 14706–14709.
3 W. L. Tsai, M. H. Huang, W. K. Lee, Y. J. Hsu, K. C. Pan, Y. H. Huang, H. C. Ting, M. Sarma, Y. Y. Ho, H. C. Hu, C. C. Chen, M. T. Lee, K. T. Wong and C. C. Wu, *Chem. Commun.*, 2015, **51**, 13662–13665.
4 S. Wang, Y. Zhang, W. Chen, J. Wei, Y. Liu and Y. Wang, *Chem. Commun.*, 2015, **51**, 11972–11975.
5 B. Minaev, G. Baryshnikov and H. Agren, *Phys. Chem. Chem. Phys.*, 2014, **16**, 1719–1758.
6 Y. Tao, K. Yuan, T. Chen, P. Xu, H. Li, R. Chen, C. Zheng, L. Zhang and W. Huang, *Adv. Mater.*, 2014, **26**, 7931–7958.
7 S. Xu, R. Chen, C. Zheng and W. Huang, *Adv. Mater.*, 2016, **28**, 9920–9940.
8 K. Nasu, T. Nakagawa, H. Nomura, C. J. Lin, C. H. Cheng, M. R. Tseng, T. Yasuda and C. Adachi, *Chem. Commun.*, 2013, **49**, 10385–10387.
9 J. Z. Fan, L. L. Lin and C. K. Wang, *Chem. Phys. Lett.*, 2016, **652**, 16–21.
10 H. Tsujimoto, D.-G. Ha, G. Markopoulos, H. S. Chae, M. A. Baldo and T. M. Swager, *J. Am. Chem. Soc.*, 2017, **139**, 4894–4900.
11 L. Lin, Z. Wang, J. Fan and C. Wang, *Org. Electron.*, 2017, **41**, 17–25.
12 Q. Zhang, H. Kuwabara, W. J. Potscavage Jr, S. Huang, Y. Hatae, T. Shibata and C. Adachi, *J. Am. Chem. Soc.*, 2014, **136**, 18070–18081.
13 L. Yao, B. Yang and Y. Ma, *Sci. China: Chem.*, 2014, **57**, 335–345.
14 X. Tang, Q. Bai, Q. Peng, Y. Gao, J. Li, Y. Liu, L. Yao, P. Lu, B. Yang and Y. Ma, *Chem. Mater.*, 2015, **27**, 7050–7057.
15 D. Hu, L. Yao, B. Yang and Y. Ma, *Philos. Trans. R. Soc., A*, 2015, **373**, 20140318.
16 Y. Wang, G. Zhang, M. Gao, Y. Cai, C. Zhan, Z. Zhao, D. Zhang and B. Z. Tang, *Faraday Discuss.*, 2017, **196**, 9–30.
17 F. Bu, R. Duan, Y. Xie, Y. Yi, Q. Peng, R. Hu, A. Qin, Z. Zhao and B. Z. Tang, *Angew. Chem., Int. Ed.*, 2015, **54**, 14492–14497.
18 Y. Hong, J. W. Lam and B. Z. Tang, *Chem. Soc. Rev.*, 2011, **40**, 5361–5388.
19 J. Hu, X. Zhang, D. Zhang, X. Cao, T. Jiang, X. Zhang and Y. Tao, *Dyes Pigm.*, 2017, **137**, 480–489.

20 M. Zambianchi, E. Benvenuti, C. Bettini, C. Zanardi, R. Seeber, D. Gentili, M. Cavallini, M. Muccini, V. Biondo, C. Soldano, G. Generali, S. Toffanin and M. Melucci, *J. Mater. Chem. C*, 2016, **4**, 9411–9417.
21 I. H. Lee, W. Song and J. Y. Lee, *Org. Electron.*, 2016, **29**, 22–26.
22 B. Huang, Z. Yin, X. Ban, Z. Ma, W. Jiang, W. Tian, M. Yang, S. Ye, B. Lin and Y. Sun, *J. Lumin.*, 2016, **172**, 7–13.
23 Y. Gao, A. Obolda, M. Zhang and F. Li, *Dyes Pigm.*, 2017, **139**, 644–650.
24 R. Englman and J. Jortner, *Mol. Phys.*, 1970, **18**, 145–164.
25 X. Han, Q. Bai, L. Yao, H. Liu, Y. Gao, J. Li, L. Liu, Y. Liu, X. Li, P. Lu and B. Yang, *Adv. Funct. Mater.*, 2015, **25**, 7521–7529.
26 H. Sun, S. Zhang, C. Zhong and Z. Sun, *J. Comput. Chem.*, 2016, **37**, 684–693.
27 T. J. Penfold, *J. Phys. Chem. C*, 2015, **119**, 13535–13544.
28 J. Z. Fan, S. Qiu, L. L. Lin and C. K. Wang, *Chin. J. Chem. Phys.*, 2016, **29**, 291–296.
29 T. Chen, L. Zheng, J. Yuan, Z. An, R. Chen, Y. Tao, H. Li, X. Xie and W. Huang, *Sci. Rep.*, 2015, **5**, 10923.
30 S. Huang, Q. Zhang, Y. Shiota, T. Nakagawa, K. Kuwabara, K. Yoshizawa and C. Adachi, *J. Chem. Theory Comput.*, 2013, **9**, 3872–3877.
31 J. Fan, L. Cai, L. Lin and C. K. Wang, *J. Phys. Chem. A*, 2016, **120**, 9422–9430.
32 L. W. Chung, W. Sameera, R. Ramozzi, A. J. Page, M. Hatanaka, G. P. Petrova, T. V. Harris, X. Li, Z. Ke, F. Liu, H. B. Li, L. Ding and K. Morokuma, *Chem. Rev.*, 2015, **115**, 5678–5796.
33 M. J. Frisch, G. W. Trucks, H. B. Schlegel, G. E. Scuseria, M. A. Robb, J. R. Cheeseman, G. Scalmani, V. Barone, B. Mennucci, G. A. Petersson, H. Nakatsuji, M. Caricato, X. Li, H. P. Hratchian, A. F. Izmaylov, J. Bloino, G. Zheng, J. L. Sonnenberg, M. Hada, M. Ehara, K. Toyota, R. Fukuda, J. Hasegawa, M. Ishida, T. Nakajima, Y. Honda, O. Kitao, H. Nakai, T. Vreven, J. A. Montgomery Jr., J. E. Peralta, F. Ogliaro, M. J. Bearpark, J. Heyd, E. N. Brothers, K. N. Kudin, V. N. Staroverov, R. Kobayashi, J. Normand, K. Raghavachari, A. P. Rendell, J. C. Burant, S. S. Iyengar, J. Tomasi, M. Cossi, N. Rega, N. J. Millam, M. Klene, J. E. Knox, J. B. Cross, V. Bakken, C. Adamo, J. Jaramillo, R. Gomperts, R. E. Stratmann, O. Yazyev, A. J. Austin, R. Cammi, C. Pomelli, J. W. Ochterski, R. L. Martin, K. Morokuma, V. G. Zakrzewski, G. A. Voth, P. Salvador, J. J. Dannenberg, S. Dapprich, A. D. Daniels, O. Farkas, J. B. Foresman, J. V. Ortiz, J. Cioslowski and D. J. Fox, *Gaussian 09*, Gaussian, Inc, 2009.
34 J. R. Reimers, *J. Chem. Phys.*, 2001, **115**, 9103–9109.
35 H. Ma, W. Shi, J. Ren, W. Li, Q. Peng and Z. Shuai, *J. Phys. Chem. Lett.*, 2016, **7**, 2893–2898.
36 Q. Peng, Q. Shi, Y. Niu, Y. Yi, S. Sun, W. Li and Z. Shuai, *J. Mater. Chem. C*, 2016, **4**, 6829–6838.
37 T. Zhang, H. Ma, Y. Niu, W. Li, D. Wang, Q. Peng, Z. Shuai and W. Liang, *J. Phys. Chem. C*, 2015, **119**, 5040–5047.
38 D. Fan, Y. Yi, Z. Li, W. Liu, Q. Peng and Z. Shuai, *J. Phys. Chem. A*, 2014, **119**, 5233–5240.
39 Y. Niu, Q. Peng, C. Deng, X. Gao and Z. Shuai, *J. Phys. Chem. A*, 2010, **114**, 7817–7831.
40 T. Lu and F. Chen, *J. Comput. Chem.*, 2012, **33**, 580–592.
41 E. R. Johnson, S. Keinan, P. Mori-Sánchez, J. Contreras-García, A. J. Cohen and W. Yang, *J. Am. Chem. Soc.*, 2010, **132**, 6498–6506.
42 J. Fan, L. Lin and C.-K. Wang, *J. Mater. Chem. C*, 2017, **5**, 8390–8399.
43 B. Wang, X. Wang, W. Wang and F. Liu, *J. Phys. Chem. C*, 2016, **120**, 21850–21857.
44 Q. Li and L. Blancafort, *Chem. Commun.*, 2013, **49**, 5966–5968.
45 X.-L. Peng, S. Ruiz-Barragan, Z.-S. Li, Q.-S. Li and L. Blancafort, *J. Mater. Chem. C*, 2016, **4**, 2802–2810.
46 G. Sun, Y. Zhao and W. Liang, *J. Chem. Theory Comput.*, 2015, **11**, 2257–2267.
47 X. Gao, Q. Peng, Y. Niu, D. Wang and Z. Shuai, *Phys. Chem. Chem. Phys.*, 2012, **14**, 14207–14216.
48 DALTON. A molecular electronic structure program, http://daltonprogram.org/.
49 Y. Gao, S. Zhang, Y. Pan, L. Yao, H. Liu, Y. Guo, Q. Gu, B. Yang and Y. Ma, *Phys. Chem. Chem. Phys.*, 2016, **18**, 24176–24184.